

## Forecasting the 8 April 2024 Total Solar Eclipse with Multiple Solar Photospheric Magnetograms

XIANYU LIU <sup>1</sup>, WEIHAO LIU <sup>1</sup>, WARD B. MANCHESTER IV <sup>1</sup>, DANIEL T. WELLING <sup>1</sup>,  
GÁBOR TÓTH <sup>1</sup>, TAMAS I. GOMBOSI <sup>1</sup>, MARC L. DE ROSA <sup>2</sup>, LUCA BERTELLO <sup>3</sup>,  
ALEXEI A. PEVTSOV <sup>3</sup>, ALEXANDER A. PEVTSOV <sup>3</sup>, KEVIN REARDON <sup>3</sup>, KATHRYN WILBANKS,<sup>1</sup>  
AMY REWOLDT,<sup>1</sup> AND LULU ZHAO <sup>1</sup>

<sup>1</sup>*Department of Climate and Space Sciences and Engineering, University of Michigan, Ann Arbor, MI 48109, USA*

<sup>2</sup>*Lockheed Martin Solar and Astrophysics Laboratory, Palo Alto, CA 94304, USA*

<sup>3</sup>*National Solar Observatory, Boulder, CO 80303, USA*

Submitted to ApJ

### ABSTRACT

The 8 April 2024 total solar eclipse (TSE) provides a unique opportunity to study the solar corona. This work presents our prediction of the solar corona at the time of the eclipse based on magnetohydrodynamic (MHD) modeling performed with the Alfvén Wave Solar Model-Realtime (AWSoM-R) in the Space Weather Modeling Framework, developed at the University of Michigan. We performed multiple simulations made with data input in the form of synchronic magnetograms from four sources, i.e., ADAPT-GONG, Lockheed Martin ESFAM, HipFT and NSO-NRT magnetograms. Simulations also include a higher-resolution model and a post-eclipse model incorporating newly emerged active regions. Our study fundamentally focuses on the limitations imposed by the lack of global solar observations, particularly on how these limitations affect coronal simulations. Specifically, we examine how differences among the magnetograms and the absence of observations from the east limb, due to the Sun’s rotation, impact the accuracy of the predicted coronal structures. We synthesized a variety of representative observables, including the white-light and extreme-ultraviolet images from each model, and compared them with observations. The synthesized observables show remarkable differences because of the distinct magnetic coronal topologies, which stem from the varied magnetic flux distributions and the gaps in observational coverage. Our findings emphasize the need for comprehensive and multi-satellite magnetic field observations to improve future solar corona predictions.

*Keywords:* Solar eclipses (1489), Solar corona (1483), Magnetogram (2359)

### 1. INTRODUCTION

The fascinating total solar eclipse (TSE) on 8 April 2024 gave people across the North America a rare opportunity to look at the appearance of the solar corona. During a TSE, the moon shields the radiation from the entire solar disk, thus enabling the naked eye to see the faint, commonly invisible

solar corona. The solar corona has been attracting great scientific interest since the first discovery of its extremely high temperature of more than 1 MK in the 19th century (Procter 1871). Several theories, including Alfvén wave heating (Alfvén 1942; De Pontieu et al. 2007; Tomczyk et al. 2007) and nanoflare heating theories (Parker 1983a,b), have been proposed to explain the coronal heating mechanism, yet the precise understanding of when and where these mechanisms apply is still unclear today. Coronal magnetic activities are also the origin of most space weather events, e.g., coronal mass ejections and flares, which can pose significant risks to the space environment and human society (Bolduc 2002; Schrijver 2015; Cliver et al. 2022).

Extensive observations have broadened our understanding of the solar corona. Over the past few decades, white-light and extreme-ultraviolet (EUV) imaging techniques have pioneered the coronal monitoring era. Spectroscopic observations across various wavelength bands have been used to reveal the dynamics and thermodynamics of local coronal structures. Other techniques, including radio observations and *in-situ* measurements, also contribute to our knowledge of the coronal plasma environment. Despite these advancements, TSE observations remain indispensable for advancing our understanding of the solar corona (SC), offering unique contributions through spectral line measurements in the visible and near-infrared that extend to the very low corona (e.g., Koutchmy 1994; Habbal et al. 2007, 2013; Druckmüller et al. 2014; Mikić et al. 2018; Boe et al. 2018, 2021; Zhu et al. 2024).

The growth in computational capacity and the improvements in numerical methods have driven the growth of magnetohydrodynamic (MHD) modeling of the corona (e.g., Odstrčil 1993; Groth et al. 2000; Usmanov & Goldstein 2003; Lionello et al. 2009; van der Holst et al. 2014; Feng et al. 2015; Mikić et al. 2018; Usmanov et al. 2018). Modern coronal models rely on synoptic or synchronic maps, i.e., the global photospheric radial magnetic field maps, to set boundary conditions and create a realistic corona and solar wind. These maps are produced by merging photospheric magnetic field measurements over the Carrington rotation into a single full-surface map. However, a significant challenge remains: routine photospheric magnetic field measurements are only available at the Earth’s viewing angle. Considering the evolution of those structures on the far-side disk is not trivial due to our missing observations. It remains to be answered how our current measurements limit the performance of coronal MHD models.

As mentioned in Mikić et al. (2018) predicting the 2017 TSE, the TSE opens up a unique opportunity to answer a list of science questions in solar physics. As the solar activity approaches its maximum, forecasting the 8 April 2024 TSE is significantly more challenging than the August 2017 event and potentially more meaningful. For the 2024 TSE event, we carried out a project to forecast the corona and help the public better understand the TSE through outreach events. We have developed the Space Weather Modeling Framework (SWMF<sup>1</sup>, Tóth et al. 2005, 2012) for decades, for the purpose of forecasting space weather and studying space physics. This work describes our 8 April 2024 TSE prediction based on the numerical simulations using SWMF and compares the outputs with observations. Our key objectives are exploring the ability of our tool to model the solar corona and studying how the magnetograms affect the models.

## 2. METHODS

<sup>1</sup> <https://github.com/SWMFsoftware>

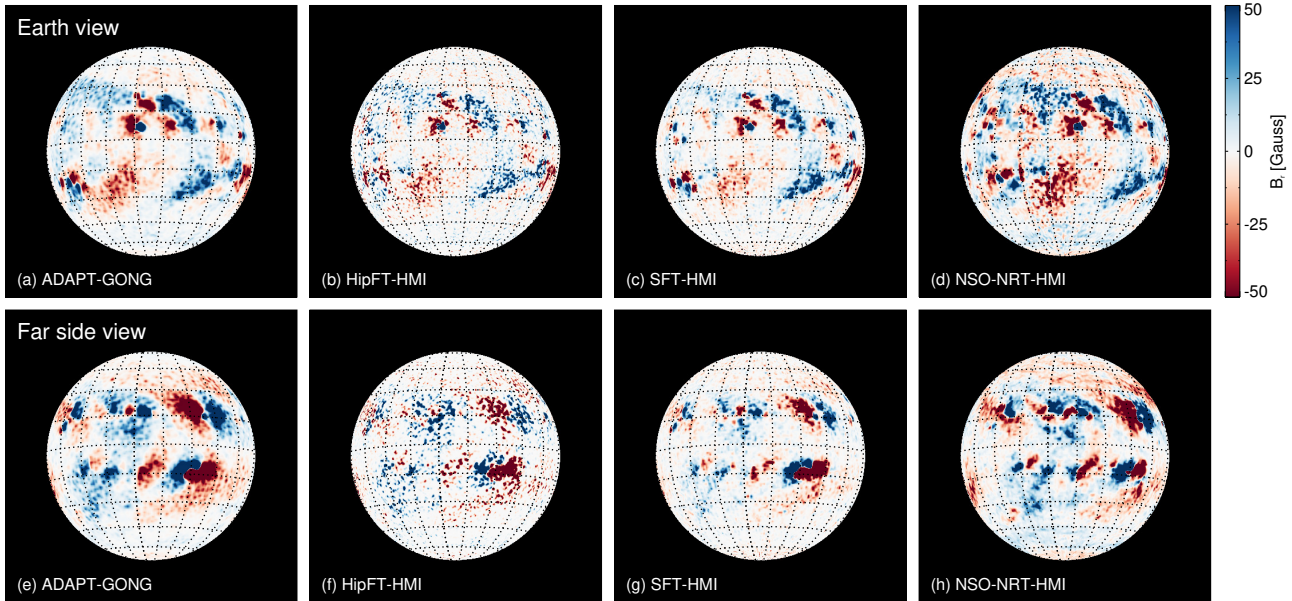


**Figure 1. Magnetograms used as the AWSOM-R boundary conditions.** The top row shows the magnetograms as viewed from the Earth’s location. The bottom row shows the same magnetograms viewed from the opposite side of Earth’s orbit. The four columns from the left to the right represent the ADAPT-GONG, HipFT-HMI, LM-ESFAM-HMI and NSO-NRT-HMI magnetograms, respectively. Each panel shares the same color bar.

### 2.1. Magnetic Maps

The first step of our prediction is to predict the photospheric magnetic field during the eclipse. Producing a magnetogram involves merging a long sequence of measurements and considering the evolution of magnetic field structures. Currently, multiple different processing methods are used. We used four magnetograms from different sources as the model input. Figure 1 shows the four magnetograms for the one-day forecast (Liu et al. 2024). The first map is the Air Force Data Assimilation Photospheric Flux Transport model using observations from the National Science Foundation (NSF) Global Oscillation Network Group (ADAPT-GONG<sup>2</sup>, Arge et al. 2010, 2011; Henney et al. 2012). The second map is produced using the High-performance Flux Transport (HipFT<sup>3</sup>, Caplan et al. 2022) and a sequence of photospheric magnetic field full-disk maps from the Helioseismic and Magnetic Imager (HMI, Scherrer et al. 2012) on board the Solar Dynamic Observatory (*SDO*, Pesnell et al. 2012). The third map is also based on HMI data, but produced using the Lockheed Martin Evolving Surface Flux Assimilation Model (LM-ESFAM<sup>4</sup>, Schrijver & De Rosa 2003). The fourth map is the near-real-time (NRT<sup>5</sup>, Sachdeva et al. 2023) map from the National Solar Observatory (NSO). While the first three maps are derived from line-of-sight magnetograms converted to pseudo-radial under the assumption that the magnetic field is radial, the fourth set of maps represents the radial magnetic field calculated from the true vector magnetic field in the photosphere. The HMI vector magnetic fields require additional vetting and are not immediately available. Thus, we used HMI data pro-

<sup>2</sup> <https://gong.nso.edu/adapt/maps>

<sup>3</sup> <https://github.com/predsci/HipFT>

<sup>4</sup> <https://lmsal.com/forecast/eclipse2024/>

<sup>5</sup> <https://doi.org/10.25668/nw0t-b078>

cessed via non-standard pipeline provided to us by the HMI/Stanford team. Vector data taken with a one-hour cadence are used. Hereafter, the four maps are referred to as the ADAPT-GONG map, HipFT-HMI map, LM-ESFAM-HMI map and NSO-NRT-HMI map, respectively.

## 2.2. *The Alfvén Wave Solar atmosphere Model*

With the four magnetograms, we construct the three-dimensional (3D) MHD models that extend from the upper chromosphere to the interplanetary space. Our MHD simulations are performed with the SWMF where we use the Alfvén Wave Solar Model (AWSoM, [van der Holst et al. 2014](#)) for the SC component. The AWSoM model solves the 3D MHD equations with the Block Adaptive Tree Solarwind-Roe-Upwind Scheme (BATS-R-US, [Powell et al. 1999](#)) in a spherical region extending from the upper chromosphere to 24 solar radii ( $R_s$ ). Recently, an updated version of the AWSoM model, AWSoM-Realtime (AWSoM-R, [Sokolov et al. 2021](#)), has been introduced to achieve higher numerical efficiency. The AWSoM-R model solves the hydrodynamics (HD) equations in a thin layer near the inner boundary of the SC domain, while above this region the model solves the 3D MHD equations in the same manner as AWSoM. This region is called the threaded-field-line region. In this work, we set the radius range of the thread-field-line region from 1.0 to 1.01  $R_s$ . The model assumes that the magnetic field in this region is potential, and that the plasma within satisfies the frozen-in condition. The model tracks the magnetic field line from the center of the boundary cells in the 3D MHD domain down to the surface and gets a list of threaded field lines. The AWSoM-R model solves the HD equations along each field line with a high resolution. The radial magnetic field and thermodynamic variables at the top of the threaded-field-line region serve as the boundary condition for the 3D MHD domain. A series of studies have validated the performance of AWSoM and AWSoM-R, particularly in reconstructing the lower corona and interplanetary solar wind structure (e.g., [Jin et al. 2012](#); [Sachdeva et al. 2019, 2021](#)).

We first used the AWSoM-R model to solve the steady-state solutions for the solar corona. Each of our models is initiated with a potential field source surface (PFSS) solution for the magnetic field and an exponentially stratified atmosphere connected to the Parker solar wind solution ([Parker 1958](#)). The PFSS field is obtained using the iterative finite-difference potential field solver (FDIPS, [Tóth et al. 2011](#)). The AWSoM-R model considers the coronal heating, radiative cooling, heat conduction, and energy partitioning between electrons and protons. The coronal heating in AWSoM-R is driven by the Alfvén wave dissipation. A detailed description can be found in [van der Holst et al. \(2014\)](#) and [Sokolov et al. \(2021\)](#).

The AWSoM-R model assumes that the Poynting flux ( $S_A$ ) of the injected wave at the boundary is proportional to the local radial magnetic field strength ( $B_\odot$ ). The proportionate  $(S_A/B)_\odot$  is an important input parameter and is set to  $1.1 \times 10^6 \text{ W m}^{-2} \text{ T}^{-1}$  as the default value in AWSoM-R, based on a series of previous work (e.g., [De Pontieu et al. 2007](#); [Sokolov et al. 2013](#), and references therein). Recent studies indicate that  $(S_A/B)_\odot$  depends on the solar cycle phase and can become smaller with higher solar activities. [Sachdeva et al. \(2021\)](#); [Huang et al. \(2023, 2024\)](#) argued that using a relatively large  $(S_A/B)_\odot$  for AWSoM-R near the solar maximum can result in unstable chromospheric evaporation. In this work, we found that the total unsigned magnetic fluxes of the four magnetograms exhibit significant differences. Therefore, different  $(S_A/B)_\odot$  values are used for the four models to achieve similar total injected energy: the  $(S_A/B)_\odot$  value for the LM-ESFAM-HMI map is set to the default  $1.1 \times 10^6 \text{ W m}^{-2} \text{ T}^{-1}$ , while for the ADAPT-GONG, HipFT-HMI and

NSO-NRT-HMI maps, the  $(S_A/B)_\odot$  value is set to  $0.7 \times 10^6 \text{ W m}^{-2} \text{ T}^{-1}$ ,  $1.0 \times 10^6 \text{ W m}^{-2} \text{ T}^{-1}$  and  $0.6 \times 10^6 \text{ W m}^{-2} \text{ T}^{-1}$ , respectively.

### 2.3. Adaptive Mesh Refinement

**Table 1.** Name, magnetogram type, the produced date of the magnetogram and the grid number of each model.

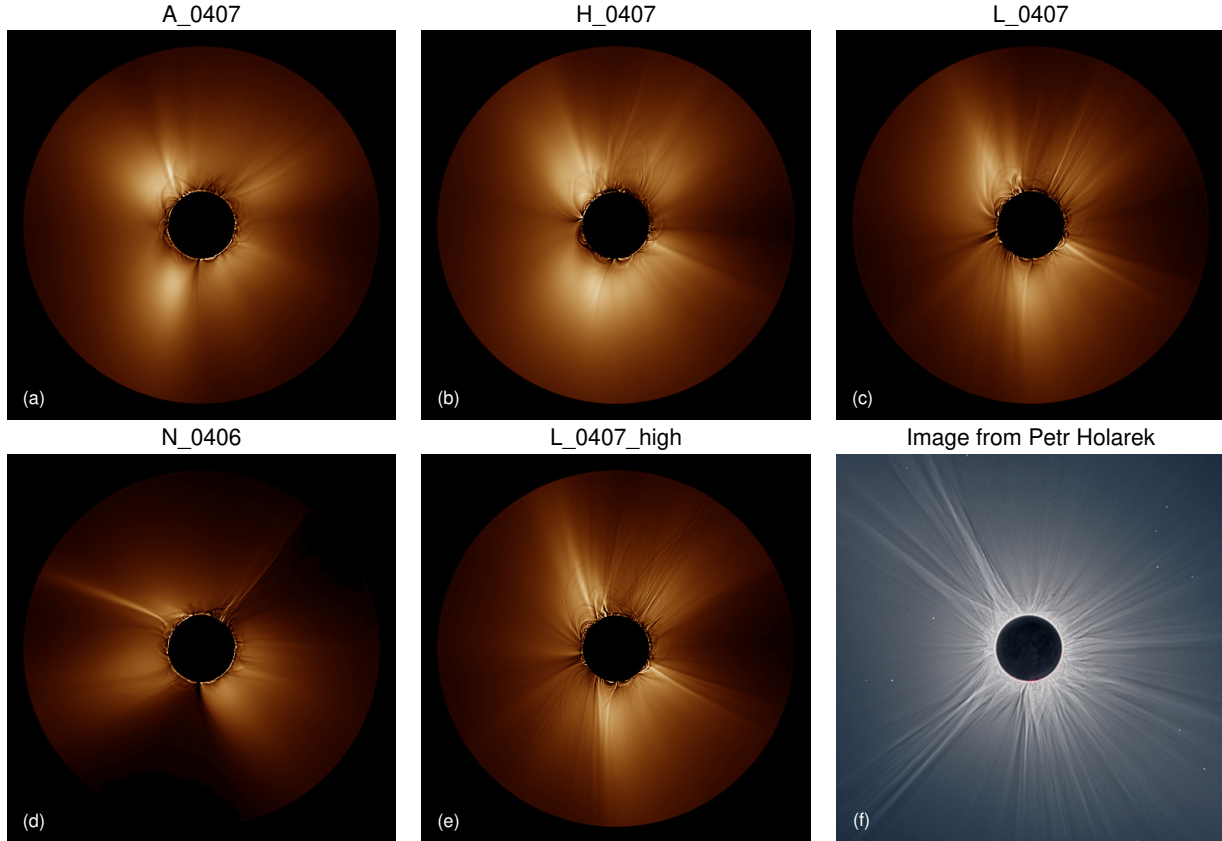
Model Name	Magnetogram	Produced Date	Grid Number
A_0407	ADAPT-GONG	April 7th	$1.97 \times 10^7$
H_0407	HipFT-HMI	April 7th	$1.97 \times 10^7$
L_0407	LM-ESFAM-HMI	April 7th	$1.97 \times 10^7$
N_0406	NSO-NRT-HMI	April 6th	$1.97 \times 10^7$
L_0407_high	LM-ESFAM-HMI	April 7th	$6.33 \times 10^7$
A_0415	ADAPT-GONG	April 15th	$1.97 \times 10^7$

Table 1 shows the prediction models we will discuss in this paper. On 7 April, that is, one day before the TSE, we first performed four simulations (A\_0407, H\_0407, L\_0407 and N\_0406) based on four up-to-date magnetograms (Liu et al. 2024). Unfortunately, a major power outage in the Boulder area interrupted the production of the current NSO-NRT-HMI magnetogram for that day. Thus, the NSO-NRT-HMI magnetogram was only available for 6 April (and earlier days). For each model, the 3D domain ( $1.01 < r < 24 R_s$ ) is decomposed with adaptive mesh refinement (AMR, Gombosi et al. 2003; Tóth et al. 2012) into blocks with  $6 \times 8 \times 8$  ( $r, \theta, \phi$ ) cells within each block. In each of the A\_0407, H\_0407, L\_0407 and N\_0406 models, we used three different refinement levels. To resolve the active regions near the solar surface, we use an angular resolution of  $0.35^\circ$  within  $(r, \theta, \phi) \in [1.01 R_s, 1.2 R_s] \times [-30^\circ, 30^\circ] \times [0^\circ, 360^\circ]$ . Outside this region and inside the  $5.5 R_s$  sphere, the angular resolution is  $0.7^\circ$ . The angular resolution outside the  $5.5 R_s$  sphere is  $1.4^\circ$ . Each of the A\_0407, H\_0407, L\_0407 and N\_0406 models contains  $1.97 \times 10^7$  grid cells. In the L\_0407\_high model, the mesh is refined by a factor of 1.5 in each direction compared to other models, and there are  $6.33 \times 10^7$  grid cells.

To study the dependence of the model on the grid resolution, we increase the grid resolution of the L\_0407 model and produce one more group of results. This model is resolved by a factor of 1.5 in each direction, with a total grid number of  $6.33 \times 10^7$  and a minimum angular grid size of  $0.23^\circ$ . As we will mention below in Section 3.1, our magnetograms for the prediction models do not contain the newly emerged active regions (ARs) on the east side of the disk. To account for the influence of these active regions in other models, we conducted an additional simulation (A\_0415) using the ADAPT-GONG magnetogram as of 15 April, one week after the TSE, when these ARs have rotated to the disk center.

## 3. RESULTS

### 3.1. TSE Predictions and Comparisons with Observations



**Figure 2. Comparison of the synthesized coronagraph images with a TSE image.** Panels (a)–(e) show results using AWSoM-R driven by five magnetograms (including a high-resolution LM variant). Panel (f) shows a TSE coronal photograph provided by Petr Holarek.

After we obtain the model outputs, we synthesize white-light and EUV images. Figure 2 shows the synthesized white-light images of the five models in panels (a)–(e) along with an actual eclipse image from Petr Holarek in panel (f). Among the four models with lower resolutions, the L\_0407 model (LM-ESFAM-HMI) is arguably the most comparable prediction. Figure 3 plots the white light image synthesized from the L\_0407 model and the 3D magnetic field. We identify five pseudo-streamers (PS1, PS2, PS3, PS4 and PS5) and a coronal loop (CL) from the 3D magnetic field, and label these structures in both panels of Figure 3. Comparing panels (c) and (e) in Figure 2, one can learn that the L\_0407\_high model predicts structures more accurately than L\_0407. Therefore, a higher resolution can help improve the sharpness of the white-light image and the prediction performance. The N\_0406 (NSO-NRT-HMI) model can predict a gap in coronal structures near the south pole, which is present in the observed corona. None of the other models shows this gap. The performance of the N\_0406 model can probably be affected by a one-day delay in production of an up-to-date map.

### 3.2. Magnetic Topology Behind Coronal Observables

The intricate patterns in panels (a)–(d) of Figure 2 prompt a deeper exploration into their origins. The white-light intensity patterns reflect the coronal plasma density. Due to the frozen-in condition

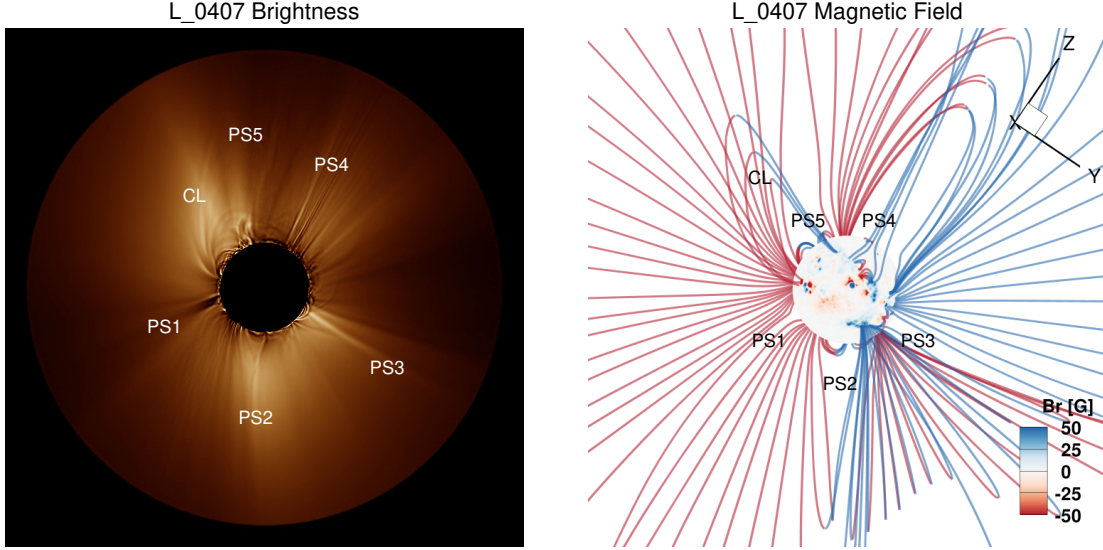


**Figure 3.** The coronagraph image synthesized from the L\_0407 model and the 3D magnetic field. The left panel shows the coronagraph image synthesized from the L\_0407 model. The right panel presents the 3D magnetic field in the model. The labeled features in the coronagraph image correspond to five streamers and a coronal loop labeled in the right panel.

in the corona, the density distribution is controlled by the magnetic field morphology. Here, we choose two parts of the white-light images in Figure 2 and study their dependence on the models.

Figure 4 provides a zoomed-in view for the upper-left part of the white-light images, along with the density and magnetic field in the plane of the sky (POS) and the photospheric magnetic field viewed from the left side of the image plane. Images from the A\_0407, H\_0407, and L\_0407 models exhibit similar patterns, while N\_0406 shows a thin and outstretching bright structure. The POS density distributions show that patterns in the A\_0407, H\_0407, and L\_0407 images originate from the large-scale loops in these three models. Figure 4(h) reveals that the bright long plume in Figure 4(d) corresponds to an outstretched structure with relatively high density. A closer look at Figure 4( $\ell$ ) and (p) finds that the local high density is generated by a pseudo-streamer. To explain the different topologies, we dive into the connection between the coronal magnetic field and the magnetograms. We use  $P_{1,2,3,4}$  to label four magnetic poles in the magnetogram in Figure 4(p), in which  $P_{1,3}$  are negative poles and  $P_{2,4}$  are positive poles.  $P_{1,2,3}$  are the three foot points of the pseudo-streamer. The magnetic field lines between the poles show that parts of  $P_{1,3}$  are connected with  $P_2$ , while other parts produce open fluxes. This indicates that the total negative fluxes are larger than the positive fluxes in this local region. In other models, magnetic poles can be identified similar to  $P_{1,2,3,4}$  but with different sizes and strengths. The most essential feature is that the counterpart of  $P_1$  in each of the other models is much weaker than  $P_1$ . In this way, the total negative fluxes are not sufficient to override the positive fluxes, thus unable to form a pseudo-streamer. The comparison between the two cases demonstrates that the different topologies are due to the different local balance of positive and negative fluxes.

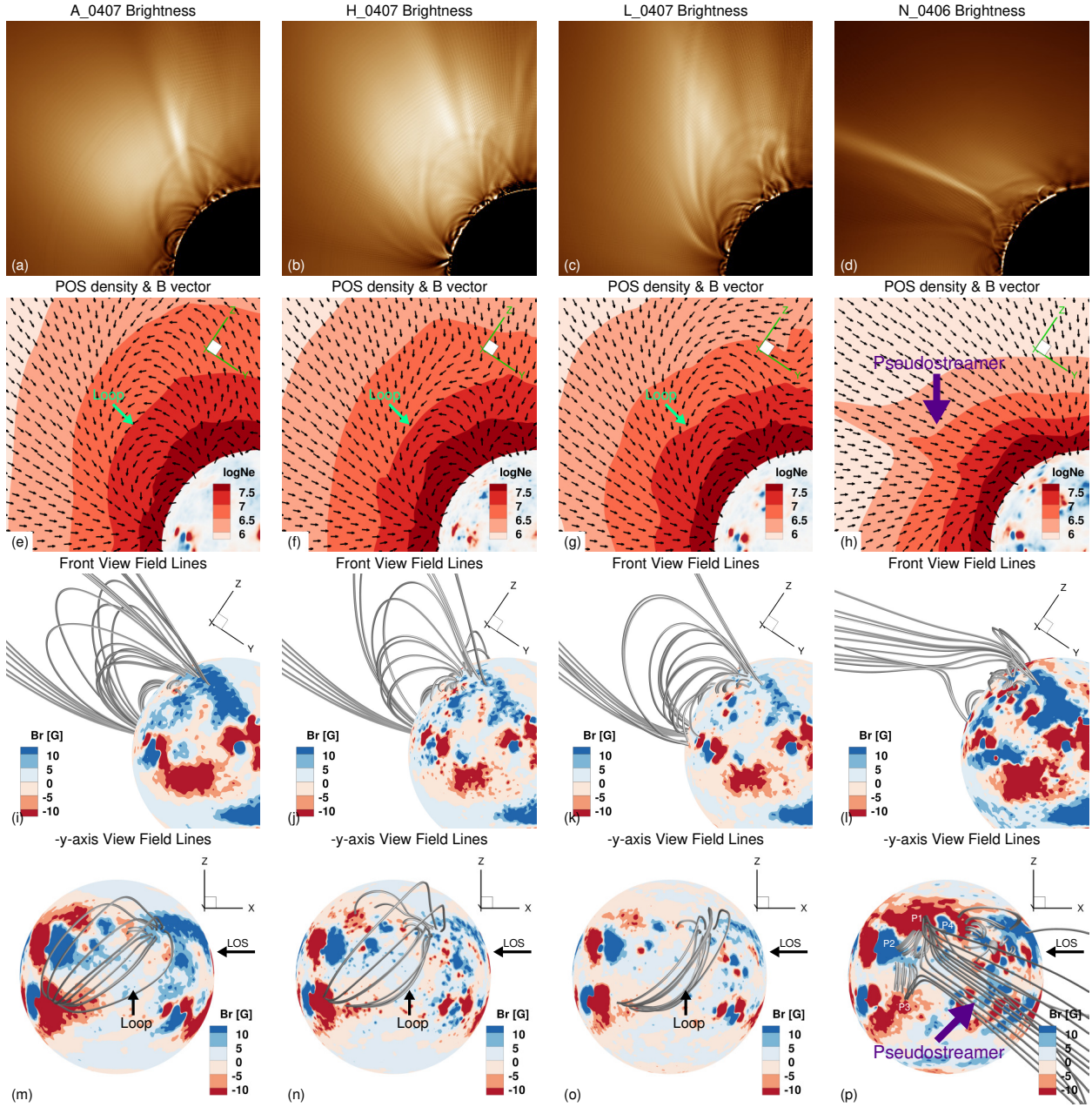


**Figure 4. Structural reasons for coronal image differences.** The top row shows the upper-left part of the synthesized white-light images of each model. The second row shows the density and the tangential magnetic field direction on the image plane. The third row shows the radial magnetic field map with the modeled 3D field lines. The first three rows share the same viewing angle. The bottom row presents the same 3D magnetic field lines as in the third row but viewed from the negative  $y$ -axis. These four columns represent A\_0407, H\_0407, L\_0407 and N\_0407 models, respectively. The loops in the POS magnetic field in panels (e), (f) and (g) correspond to the loops seen with the left view in panels (m), (n) and (o), respectively. The stretching structure in the POS density map in panel (h) corresponds to the pseudo-streamer in panel (p). The footpoints of the pseudo-streamer in panel (p) are labeled by  $P_{1,2,3}$ .

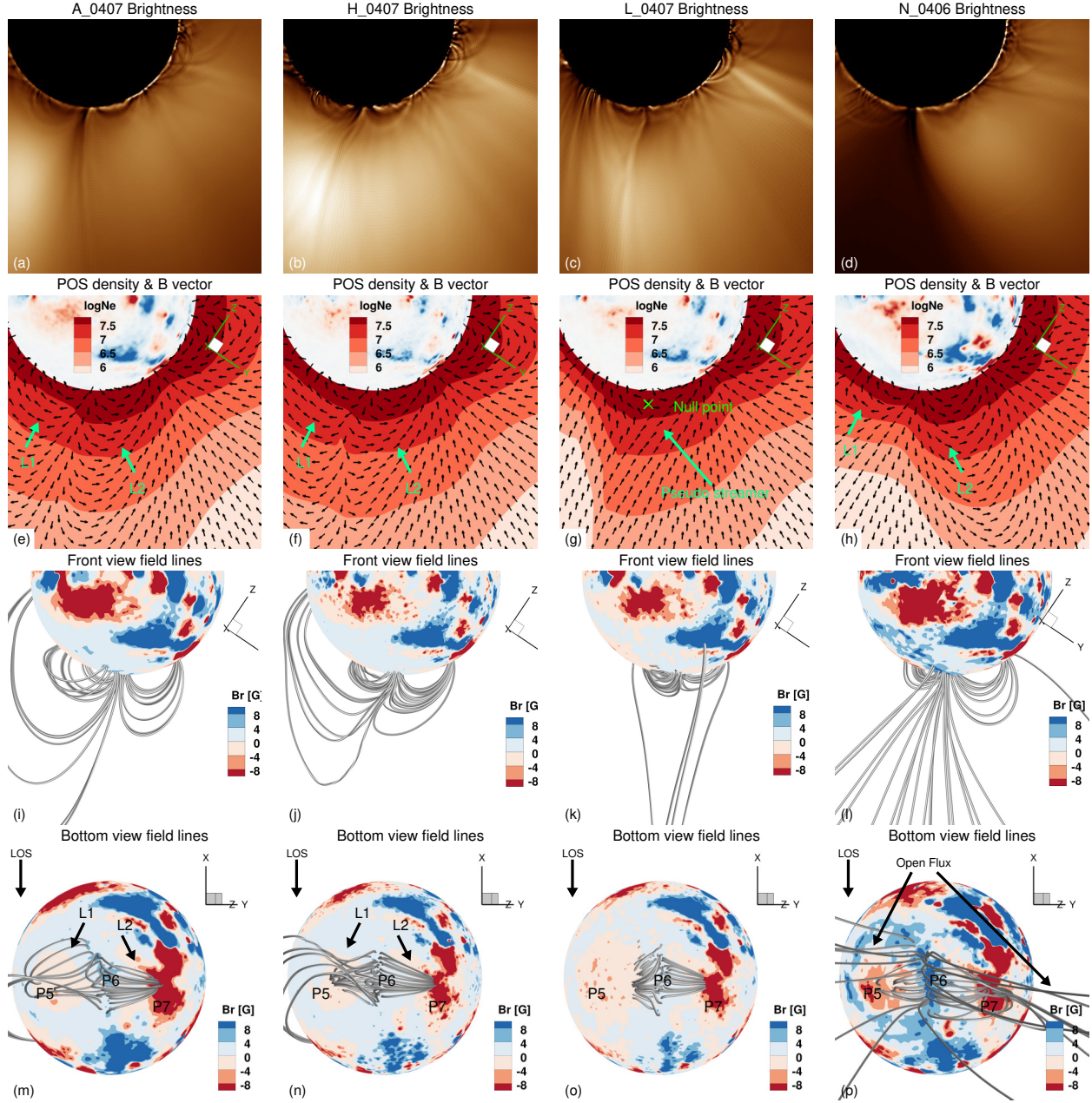


**Figure 5. Structural reasons for coronal image differences.** Similar to Figure 4, but here it is for the bottom part of the models. The bottom row shows the 3D magnetic topology viewed from the south pole. The loops  $L_{1,2}$  in each of panels (e), (f) and (h) correspond to those in each of panels (m), (n) and (o), respectively. The dark region in the white-light image of the N\_0407 model in panel (d) corresponds to the open flux region in panels (l) and (p). One can see a pseudo-streamer in the L\_0407 model in panels (g) and (k) with the null point labeled in panel (g).

We then choose the bottom part of the white-light images for analysis, as shown in Figure 5, which is similar to Figure 4, while the bottom row shows a view of the model's south pole. From the second row of Figure 5, one can find three kinds of magnetic topologies: 1. In panels (e) and (f), the A\_0407 and H\_0407 models contain two loops  $L_{1,2}$ . 2. The L\_0407 model has a pseudo-streamer with its

null point labeled in panel (g). 3. The N\_0406 model in panel (g) also has loops  $L_{1,2}$  similar to those in panels (e) and (f), while in the middle of the two loops one can see a wide open-field region. We use the bottom row of Figure 5 to help explain these different structures. In each of the panels (m), (n), (o) and (p), we label three magnetic poles with  $P_{5,6,7}$ , among which the  $P_5$  indicates the solar south pole. The loops  $L_{1,2}$  in panels (m) and (n) are the simple connections between the three poles. In panel (o), the positive fluxes in  $P_6$  are significantly weaker than the negative fluxes in  $P_{5,7}$ . Thus, the negative fluxes override the positive fluxes and form the pseudo-streamer, similar to the structure in panel (p). In Figure 5(p), the  $P_6$  of the N\_0406 is much stronger than the  $P_6$  of other maps. Therefore, the opposing poles  $P_{5,7}$  do not contain enough fluxes to close all the field lines of  $P_6$ . The remaining fluxes of  $P_6$  form the large open flux region with low density. One can learn that the local balance of positive and negative fluxes determines the topology of magnetic fields, which is similar to the situation in Figure 4.

Our analysis above reveals that the diversity of white-light patterns is due to the different distributions of magnetic fluxes in the four magnetograms. In the regions we examined, the maps exhibit similar magnetic polarity distributions, while the local balances of positive and negative magnetic fluxes are different for the maps. This underscores the crucial role of magnetic flux distribution in shaping the topology of the 3D magnetic field, even when the polarity patterns of the magnetograms are similar.

### 3.3. Missing Observations of the East Limb

The EUV image from the Atmospheric Imaging Assembly (AIA, [Lemen et al. 2012](#)) on board *SDO* is another observable on which we focus. As shown in Figure 6, the synthesized images match the observations well in terms of the general intensity distribution and the positions of most active regions. However, discrepancies can be found in some local areas. An example is the active regions on the east limb. The *SDO*/AIA observed images clearly show an out-stretching active region (AR1) on the east limb, whereas the synthetic images do not show identifiable structures at the corresponding position of AR1. We notice that none of our models can successfully predict the occurrence of AR1. This discrepancy stems from the lack of magnetic field observations in AR1. Due to the rotation of the Sun, the observations miss the structures located near the east limb within more than half a Carrington rotation before the eclipse. During this period, the photospheric field of AR1 could have evolved significantly, which cannot be accounted for by our magnetograms. In contrast, structures near the west limb have not been missed in the observation for a long time gap, which means the magnetograms contain more recent information on these structures. As a result, our predicted coronal loop (labeled as CL in Figure 6) on the west limb shows a morphology that closely matches the observed image, although one can still find some discrepancies between the predicted and observed channel intensities.

To better understand the influence of missing observations, we compare the A\_0407 model, which was based on pre-eclipse data, and the A\_0415 model, which incorporated post-eclipse data when the AR1 had rotated to the disk center. Figure 7 presents the POS density and magnetic field, along with the magnetic field in the left view of the two models. As shown in Figure 4, the A\_0407 model contains a large-scale loop on the east limb. In contrast, the A\_0415 model exhibits a pseudo-steamer structure in Figure 7(d), indicating a substantial change in the magnetic field topology due to the newly-emerged AR1. The comparison highlights how missing observations of the east limb would affect the magnetic topology in coronal models. As pointed out by [Pangestu et al. \(2023\)](#), interpreting

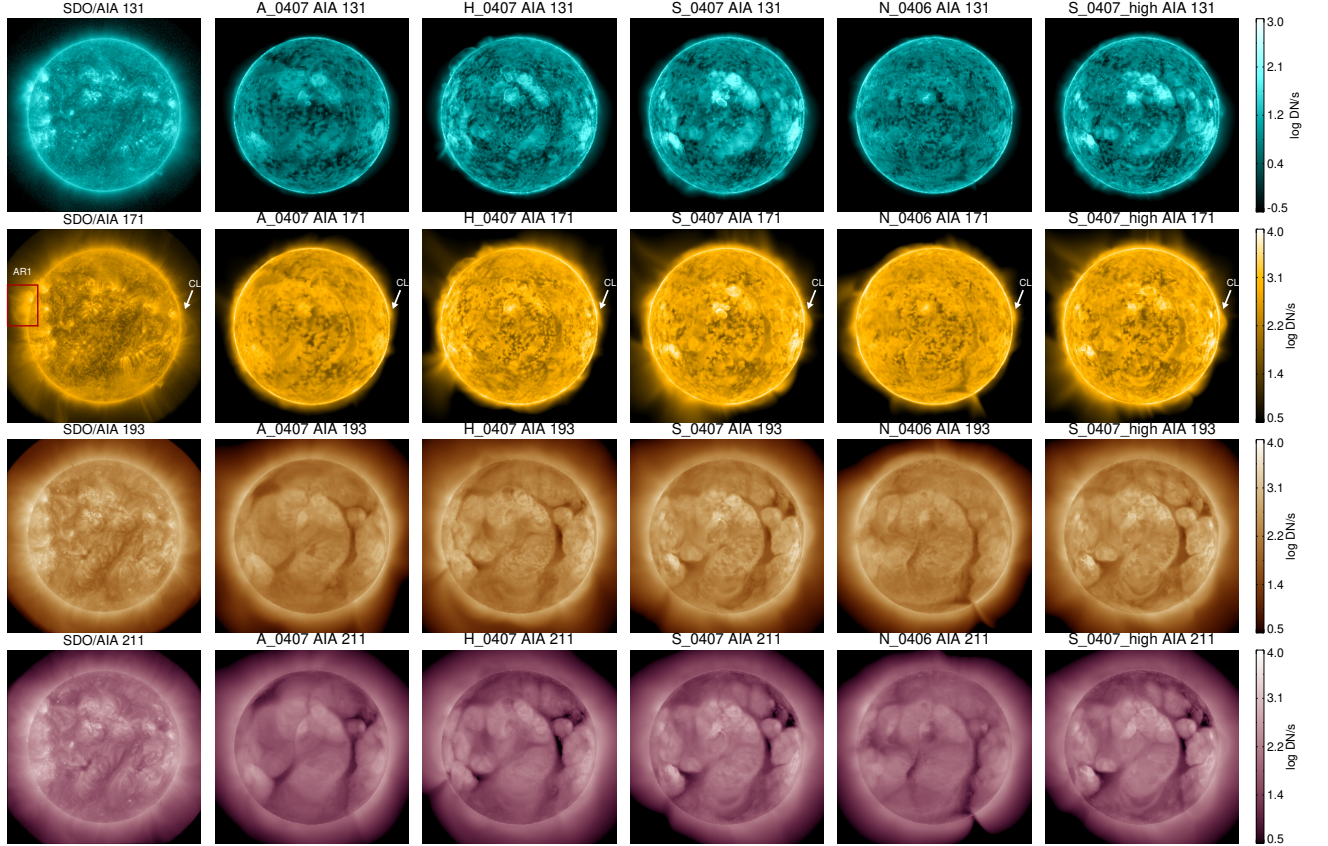


**Figure 6.** Comparison of synthesized AIA images with corresponding *SDO/AIA* observations. The first column shows the intensity images of *SDO/AIA* 131, 171, 193 and 211 Å channels from the top to the bottom panels. The following five columns show the AIA images of corresponding channels synthesized from the five prediction models. Each column contains the images of one model. The intensities in all panels are shown in the logarithmic scale.

the east limb structures has been a challenge in space weather predictions, especially when it comes to the difficulty of predicting associated flares. Our finding suggests that the impact from the missing observation can further extend to the magnetic field topology on a large spatial scale.

#### 4. SUMMARY AND DISCUSSION

In this work, we used four synchronic maps to construct prediction models for the 8 April TSE. The synthetic images of the models show significant discrepancies with the observed corona, which mainly originate from the differences in the maps. We chose several areas in these models and analyzed the connection between the simulation results and the maps. The result shows that the 3D magnetic field topology is highly sensitive to the local distribution of the magnetic flux in the magnetogram. Even when the maps exhibit similar polarity distribution patterns, differences in the magnetic flux distributions can still produce distinct magnetic topologies. We also noticed that the missing observation of the east limb strongly affects the simulation of related structures.

Our findings underscore the critical role of accurate magnetogram data in coronal modelings. The discrepancies among maps are essentially due to two factors: (1) The limited viewing angle of magnetic field measurements and (2) the different data processing methods applied to these magne-

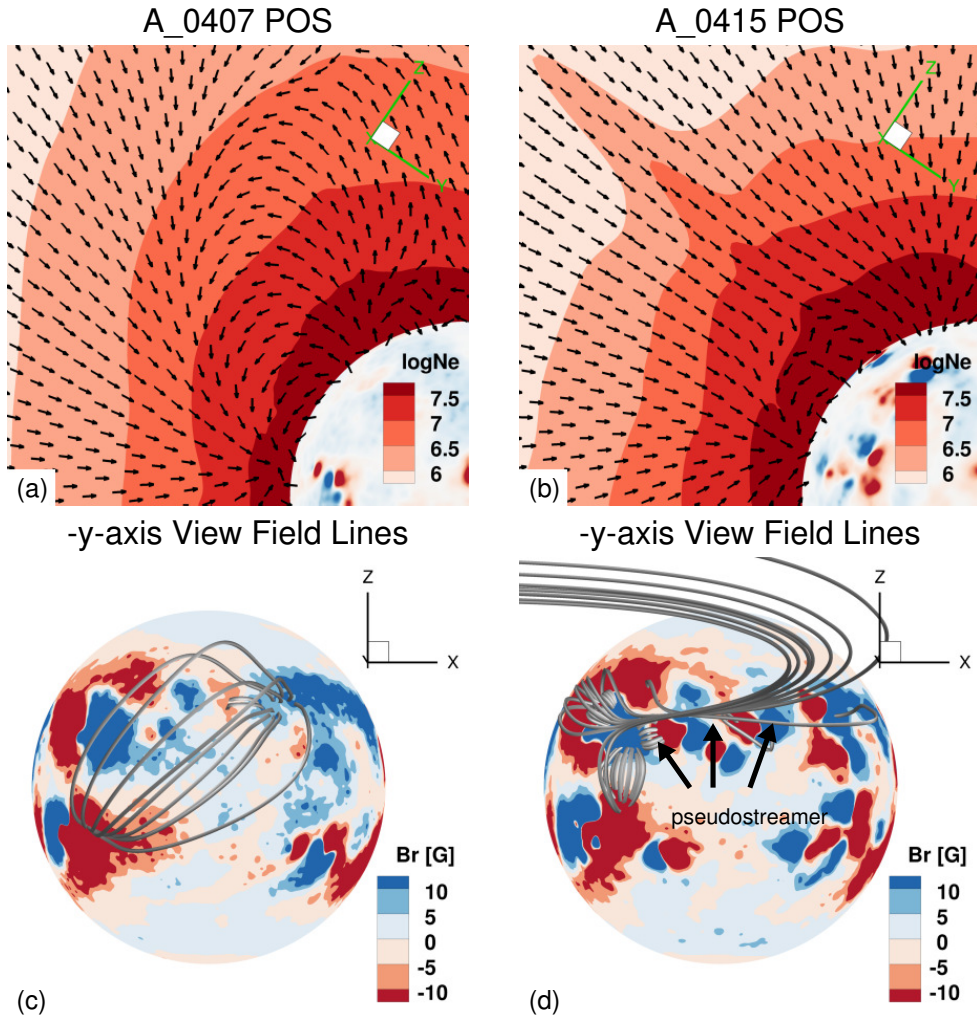


**Figure 7. Comparison of the simulation results in A\_0407 and A\_0415 using two different up-to-date maps.** The top row shows the POS density, magnetogram and coronal magnetic field direction for the A\_0407 and A\_0415 models, while the bottom row shows the magnetic field seen from the negative  $y$ -axis. The A\_0407 model produces a large-scale loop, while the A\_0415 model produces a pseudo-streamer.

tograms. Notably, the diversity in processing methods is, to some extent, a consequence of the first issue. Supposing that we had instruments to observe the entire solar surface, there would be much less necessity to assimilate the data over a range of time.

One of the key implications of our work lies in the realm of operational space weather modeling. For decades, space weather modeling and forecasting have been major objectives of the SWMF model (Gombosi et al. 2021). While this study demonstrates the capability to perform high-resolution coronal simulations well-compared with observations, the consistency of model results with magnetogram data and processing method is also indispensable to achieve a stable and reliable coronal model. The variability of the model output introduced by the data and processing methods, as we mentioned earlier, poses an obstacle to operational application. Our previous work in Sachdeva et al. (2023) studied the synthetic AIA images and solar wind conditions at 1 au in several models based on different magnetograms, whereas in this work we mainly focus on the magnetic field topology in the lower

corona and its connection to the coronal appearance at the time of a TSE. Future work is needed to better understand how the magnetic field data and processing affect the coronal models.

Another important implication of our work is the necessity for multi-satellite measurements of the solar magnetic field. Currently, the Polarimetric and Helioseismic Imager (Solanki et al. 2020) on board the Solar Orbiter mission (Müller et al. 2020) can measure the photospheric magnetic field from another viewing angle, while its ability to constrain the global magnetogram is limited due to the small field of view and continuously changing satellite position. Recently, the use of deep learning to derive the magnetograms on the far side has been viewed as an alternative approach (e.g., Kim et al. 2019; Jeong et al. 2022). Despite the dramatic growth of this method, more studies are still required to test its reliability or apply it to coronal models. From a long-term perspective, an optimal approach to the far-side magnetogram would be future missions capable of providing continuous, simultaneous, full-disk and direct observations from multiple viewing angles, especially the far-side and polar regions.

This work provides predictions of the eclipse using numerical techniques. We used four magnetograms and performed MHD simulations of the solar corona, synthesized white-light and EUV images and compared them to the observations. To study the differences between the models, we investigated the connection between the magnetograms and the 3D magnetic fields. Our conclusions are as follows:

1. Our AWSoM-R model is capable of simulating the solar coronal with realistic thermodynamic and magnetic field properties. The synthesized white-light and EUV images match well the observations.
2. Accurate determination of photospheric magnetogram is essential in coronal modeling. Having the same polarity centers in a magnetogram does not guarantee an identical 3D magnetic field topology. The local balancing between the positive and negative fluxes plays an important role in shaping the magnetic field. We also note that using vector magnetic field instead of pseudo-radial does have a positive impact on prediction at least in some areas of the corona.
3. Future work is required to better understand how the differences in the magnetograms and synchronic maps may affect the simulation.
4. For an ultimate goal of achieving reliable solar coronal modeling and space weather prediction, here we suggest to the community that a future concentration on the multi-spacecraft measurements of the photospheric magnetic field is necessary.

#### ACKNOWLEDGMENTS

This work is primarily supported by the NASA LWS Strategic Capabilities grant 80NSSC22K0892 (SCEPTER) and the NASA SWxC grant 80NSSC23M0191 (CLEAR). We thank the *SDO*/HMI science project for providing the original full-disk magnetograms used to create synoptic maps in this study. The authors thank the HipFT model development team in Predictive Science Inc. We thank the ADAPT model development team, supported by the Air Force Research Laboratory (AFRL) along with the Air Force Office of Scientific Research (AFOSR) tasks 18RVCOR126 and 22RVCOR012. Data used in the ADAPT model were acquired by GONG instruments operated by NISP/NSO/AURA/NSF with a contribution from NOAA. The NSO is operated by the Association of Universities for Research in Astronomy (AURA), Inc. under a cooperative agreement with the

National Science Foundation. In this paper, the views expressed are those of the authors and do not reflect the official guidance or position of the Department of Defense (DoD), the United States Air Force and the National Aeronautics and Space Administration. We also acknowledge the high-performance computing support from the Texas Advanced Computing Center (TACC) Frontera at the University of Texas at Austin (Stanzione et al. 2020), and the NASA supercomputing system Pleiades as part of the NASA High-End Computing (HEC) Program through the NASA Advanced Supercomputing (NAS) Division at Ames Research Center.

## APPENDIX

### A. THE LM-ESFAM MODEL

The ESFAM model, as originally developed at Lockheed Martin, is described in Schrijver (2001). This “pure simulation” model enabled the evolution of the photospheric magnetic field of cool Sun-like stars to be modeled. When run with the parameter set applicable for the Sun, the model provides time series of full-Sun magnetic maps throughout multiple sunspot cycles. The emergence of flux onto the model photosphere is based on empirical descriptions that apply to the full spectrum of bipoles, ranging from active regions on the large end to ephemeral regions on the small end. Once flux has been inserted into the model, the flux is evolved in time due to parametrized descriptions of the large-scale differential rotation and meridional flow patterns. The dispersal of flux from convective flow patterns is also captured.

In assimilation mode, described in Schrijver & De Rosa (2003), observed magnetogram images from HMI are inserted into the model in order to capture the actual locations of bipolar regions. The state of the assimilation model is sampled every six hours, and the magnetic maps at these times are publicly available. For the study presented here, starting about a month prior to the date of the TSE, the assimilation model was run forward in time until the TSE date, at which time the state of the model was captured.

## REFERENCES

- Alfvén, H. 1942, *Nature*, 150, 405,  
doi: [10.1038/150405d0](https://doi.org/10.1038/150405d0)
- Arge, C. N., Henney, C. J., Koller, J., et al. 2010, *AIP conference proceedings*, 1216, 343,  
doi: [10.1063/1.3395870](https://doi.org/10.1063/1.3395870)
- . 2011, 5th international conference of numerical modeling of space plasma flows (astronom 2010), 444, 99
- Boe, B., Habbal, S., Downs, C., & Druckmüller, M. 2021, *ApJ*, 912, 44,  
doi: [10.3847/1538-4357/abea79](https://doi.org/10.3847/1538-4357/abea79)
- Boe, B., Habbal, S., Druckmüller, M., et al. 2018, *ApJ*, 859, 155, doi: [10.3847/1538-4357/aabfb7](https://doi.org/10.3847/1538-4357/aabfb7)
- Bolduc, L. 2002, *Journal of Atmospheric and Solar-Terrestrial Physics*, 64, 1793,  
doi: [10.1016/S1364-6826\(02\)00128-1](https://doi.org/10.1016/S1364-6826(02)00128-1)
- Caplan, R., Upton, L., Linker, J., et al. 2022, *Authorea Preprints*,  
doi: [10.1002/essoar.10509134.1](https://doi.org/10.1002/essoar.10509134.1)
- Cliver, E. W., Schrijver, C. J., Shibata, K., & Usoskin, I. G. 2022, *Living Reviews in Solar Physics*, 19, 2, doi: [10.1007/s41116-022-00033-8](https://doi.org/10.1007/s41116-022-00033-8)
- De Pontieu, B., McIntosh, S. W., Carlsson, M., et al. 2007, *Science*, 318, 1574,  
doi: [10.1126/science.1151747](https://doi.org/10.1126/science.1151747)
- De Pontieu, B., McIntosh, S., Carlsson, M., et al. 2007, *Science*, 318, 1574,  
doi: [10.1126/science.1151747](https://doi.org/10.1126/science.1151747)
- Druckmüller, M., Habbal, S. R., & Morgan, H. 2014, *ApJ*, 785, 14,  
doi: [10.1088/0004-637X/785/1/14](https://doi.org/10.1088/0004-637X/785/1/14)

- Feng, L., Wang, Y., Shen, F., et al. 2015, *Astrophys. J.*, 812, 70, doi: [10.1088/0004-637X/812/1/70](https://doi.org/10.1088/0004-637X/812/1/70)
- Gombosi, T. I., De Zeeuw, D. L., Powell, K. G., et al. 2003, *Space Plasma Simulation*, 247, doi: [10.1007/3-540-36530-3\\_12](https://doi.org/10.1007/3-540-36530-3_12)
- Gombosi, T. I., Chen, Y., Glocer, A., et al. 2021, *Journal of Space Weather and Space Climate*, 11, 42, doi: [10.1051/swsc/2021020](https://doi.org/10.1051/swsc/2021020)
- Groth, C., De Zeeuw, D. L., Gombosi, T., & Powell, K. 2000, *J. Geophys. Res.*, 105, 25053, doi: [10.1029/2000JA900093](https://doi.org/10.1029/2000JA900093)
- Habbal, S. R., Morgan, H., Druckmüller, M., et al. 2013, *SoPh*, 285, 9, doi: [10.1007/s11207-012-0115-5](https://doi.org/10.1007/s11207-012-0115-5)
- Habbal, S. R., Morgan, H., Johnson, J., et al. 2007, *ApJ*, 663, 598, doi: [10.1086/518403](https://doi.org/10.1086/518403)
- Henney, C., Toussaint, W., White, S., & Arge, C. 2012, *Space Weather*, 10, doi: [10.1029/2011SW000748](https://doi.org/10.1029/2011SW000748)
- Huang, Z., Tóth, G., Sachdeva, N., & van der Holst, B. 2024, *ApJ*, 965, 1, doi: [10.3847/1538-4357/ad32ca](https://doi.org/10.3847/1538-4357/ad32ca)
- Huang, Z., Tóth, G., Sachdeva, N., et al. 2023, *ApJL*, 946, L47, doi: [10.3847/2041-8213/acc5ef](https://doi.org/10.3847/2041-8213/acc5ef)
- Jeong, H.-J., Moon, Y.-J., Park, E., Lee, H., & Baek, J.-H. 2022, *ApJS*, 262, 50, doi: [10.3847/1538-4365/ac8d66](https://doi.org/10.3847/1538-4365/ac8d66)
- Jin, M., Manchester, W. B., van der Holst, B., et al. 2012, *ApJ*, 745, 6, doi: [10.1088/0004-637X/745/1/6](https://doi.org/10.1088/0004-637X/745/1/6)
- Kim, T., Park, E., Lee, H., et al. 2019, *Nature Astronomy*, 3, 397, doi: [10.1038/s41550-019-0711-5](https://doi.org/10.1038/s41550-019-0711-5)
- Koutchmy, S. 1994, *Advances in Space Research*, 14, 29, doi: [10.1016/0273-1177\(94\)90156-2](https://doi.org/10.1016/0273-1177(94)90156-2)
- Lemen, J. R., Title, A. M., Akin, D. J., et al. 2012, *SoPh*, 275, 17, doi: [10.1007/s11207-011-9776-8](https://doi.org/10.1007/s11207-011-9776-8)
- Lionello, R., Linker, J. A., & Mikić, Z. 2009, *ApJ*, 690, 902, doi: [10.1088/0004-637X/690/1/902](https://doi.org/10.1088/0004-637X/690/1/902)
- Liu, W., Liu, X., Wilbanks, K., et al. 2024, *CoronaCast 2024: 1-Day Forecast*, 02, Zenodo, doi: [10.5281/zenodo.10947040](https://doi.org/10.5281/zenodo.10947040)
- Mikić, Z., Downs, C., Linker, J. A., et al. 2018, *Nature Astronomy*, 2, 913, doi: [10.1038/s41550-018-0562-5](https://doi.org/10.1038/s41550-018-0562-5)
- Müller, D., St. Cyr, O. C., Zouganelis, I., et al. 2020, *A&A*, 642, A1, doi: [10.1051/0004-6361/202038467](https://doi.org/10.1051/0004-6361/202038467)
- Odstrčil. 1993, *J. Comput. Phys.*, 108, 218, doi: [10.1006/jcph.1993.1177](https://doi.org/10.1006/jcph.1993.1177)
- Pangestu, A. D., Muhamad, J., Nurzaman, M. Z., et al. 2023, *Journal of Astrophysics and Astronomy*, 44, 25, doi: [10.1007/s12036-023-09915-1](https://doi.org/10.1007/s12036-023-09915-1)
- Parker, E. N. 1958, *ApJ*, 128, 664, doi: [10.1086/146579](https://doi.org/10.1086/146579)
- . 1983a, *ApJ*, 264, 635, doi: [10.1086/160636](https://doi.org/10.1086/160636)
- . 1983b, *ApJ*, 264, 642, doi: [10.1086/160637](https://doi.org/10.1086/160637)
- Pesnell, W. D., Thompson, B. J., & Chamberlin, P. C. 2012, *SoPh*, 275, 3, doi: [10.1007/s11207-011-9841-3](https://doi.org/10.1007/s11207-011-9841-3)
- Powell, K. G., Roe, P. L., Linde, T. J., Gombosi, T. I., & De Zeeuw, D. L. 1999, *Journal of Computational Physics*, 154, 284, doi: [10.1006/jcph.1999.6299](https://doi.org/10.1006/jcph.1999.6299)
- Procter, H. R. 1871, *Nature*, 3, 468, doi: [10.1038/003468a0](https://doi.org/10.1038/003468a0)
- Sachdeva, N., van der Holst, B., Manchester, W. B., et al. 2019, *ApJ*, 887, 83, doi: [10.3847/1538-4357/ab4f5e](https://doi.org/10.3847/1538-4357/ab4f5e)
- Sachdeva, N., Tóth, G., Manchester, W. B., et al. 2021, *ApJ*, 923, 176, doi: [10.3847/1538-4357/ac307c](https://doi.org/10.3847/1538-4357/ac307c)
- Sachdeva, N., Manchester, Ward B., I., Sokolov, I., et al. 2023, *ApJ*, 952, 117, doi: [10.3847/1538-4357/acda87](https://doi.org/10.3847/1538-4357/acda87)
- Scherrer, P. H., Schou, J., Bush, R., et al. 2012, *SoPh*, 275, 207, doi: [10.1007/s11207-011-9834-2](https://doi.org/10.1007/s11207-011-9834-2)
- Schrijver, C. J. 2001, *ApJ*, 547, 475, doi: [10.1086/318333](https://doi.org/10.1086/318333)
- . 2015, *Space Weather*, 13, 524, doi: [10.1002/2015SW001252](https://doi.org/10.1002/2015SW001252)
- Schrijver, C. J., & De Rosa, M. L. 2003, *SoPh*, 212, 165, doi: [10.1023/A:1022908504100](https://doi.org/10.1023/A:1022908504100)
- Sokolov, I. V., van der Holst, B., Oran, R., et al. 2013, *ApJ*, 764, 23, doi: [10.1088/0004-637X/764/1/23](https://doi.org/10.1088/0004-637X/764/1/23)
- Sokolov, I. V., Holst, B. v. d., Manchester, W. B., et al. 2021, *ApJ*, 908, 172, doi: [10.3847/1538-4357/abc000](https://doi.org/10.3847/1538-4357/abc000)
- Solanki, S. K., del Toro Iniesta, J. C., Woch, J., et al. 2020, *A&A*, 642, A11, doi: [10.1051/0004-6361/201935325](https://doi.org/10.1051/0004-6361/201935325)
- Stanzione, D., West, J., Evans, R. T., et al. 2020, in *Practice and Experience in Advanced Research Computing 2020: Catch the Wave* (Association for Computing Machinery), 106–111, doi: [10.1145/3311790.3396656](https://doi.org/10.1145/3311790.3396656)

- Tomczyk, S., McIntosh, S. W., Keil, S. L., et al. 2007, *Science*, 317, 1192, doi: [10.1126/science.1143304](https://doi.org/10.1126/science.1143304)
- Tóth, G., van der Holst, B., & Huang, Z. 2011, *ApJ*, 732, 102, doi: [10.1088/0004-637X/732/2/102](https://doi.org/10.1088/0004-637X/732/2/102)
- Tóth, G., Sokolov, I. V., Gombosi, T. I., et al. 2005, *Journal of Geophysical Research: Space Physics*, 110, doi: [10.1029/2005JA011126](https://doi.org/10.1029/2005JA011126)
- Tóth, G., van der Holst, B., Sokolov, I. V., et al. 2012, *Journal of Computational Physics*, 231, 870, doi: [10.1016/j.jcp.2011.02.006](https://doi.org/10.1016/j.jcp.2011.02.006)
- Usmanov, A. V., & Goldstein, M. L. 2003, *J. Geophys. Res.*, 108, 1354, doi: [10.1029/2002JA009777](https://doi.org/10.1029/2002JA009777)
- Usmanov, A. V., Matthaeus, W. H., Goldstein, M. L., & Chhiber, R. 2018, *ApJ*, 865, 25, doi: [10.3847/1538-4357/aad687](https://doi.org/10.3847/1538-4357/aad687)
- van der Holst, B., Sokolov, I. V., Meng, X., et al. 2014, *ApJ*, 782, 81, doi: [10.1088/0004-637X/782/2/81](https://doi.org/10.1088/0004-637X/782/2/81)
- Zhu, Y., Habbal, S. R., Ding, A., et al. 2024, *ApJ*, 966, 122, doi: [10.3847/1538-4357/ad3424](https://doi.org/10.3847/1538-4357/ad3424)